

Volume of hyperintense inflammation (V_{HI}): a deep learning-enabled quantitative imaging biomarker of inflammation load in spondyloarthritis

Authors:

Carolyna Hepburn^{1,2} PhD

Alexis Jones^{1,3} MBBChir MD(Res)

Alan Bainbridge⁴ PhD

Coziana Ciurtin³ MBBS PhD

Juan Eugenio Iglesias^{2,5,6} PhD

Hui Zhang³ PhD

*Margaret A. Hall-Craggs^{1,7} MBBChir MD(Res)

*Timothy JP Bray^{1,2,7} MBBChir PhD

¹Centre for Medical Imaging, University College London, United Kingdom

²Centre for Medical Image Computing, University College London, United Kingdom

³Centre for Adolescent Rheumatology

⁴Department of Medical Physics, University College London Hospitals, United Kingdom

⁵Computer Science and Artificial Intelligence Laboratory, Massachusetts Institute of Technology, Boston, USA

⁶Martinos Center for Biomedical Imaging, Massachusetts General Hospital and Harvard Medical School, Boston, USA

⁷Imaging Department, University College London Hospital, United Kingdom

*Joint senior authorship

Corresponding author:

Timothy J.P. Bray, Centre for Medical Imaging, University College London

Email: t.bray@ucl.ac.uk

Running title:

Volume of hyperintense inflammation (V_{HI}) as a quantitative imaging biomarker

Abstract

Background: Short inversion time inversion recovery (STIR) MRI is widely used in clinical practice to identify and quantify inflammation in axial spondyloarthritis. However, assessment of STIR images is limited by the need for qualitative evaluation, which depends on observer experience and expertise, creating substantial variability in inflammation assessments.

Purpose: To address this problem, we developed a deep learning-enabled, semiautomated workflow for segmentation of inflammatory lesions, whereby an initial segmentation is generated automatically and a radiologist then ‘cleans’ the segmentation by removing extraneous segmented voxels. The final cleaned segmentation defines the volume of hyperintense inflammation (V_{HI}), which we propose as a quantitative imaging biomarker of inflammation load in spondyloarthritis.

Study type: Retrospective analysis of prospective dataset.

Population: 29 patients with axial spondyloarthritis undergoing MRI before and after starting biologic therapy.

Field strength/sequence: 3T MRI including STIR and T_1 -weighted spin echo sequences.

Assessment: The performance of the semiautomated workflow was compared against purely visual assessment (both manual segmentation and visual scoring) in terms of inter-observer/inter-method segmentation overlap, inter-observer agreement and assessment of response to biologic therapy.

Statistical tests: Dice coefficients for segmentation overlap, Bland-Altman analysis for agreement assessment, descriptive statistics for response evaluation.

Results: The semiautomated workflow showed superior inter-observer segmentation overlap than purely manual segmentation (Dice score 0.84 versus 0.56) and superior performance against a composite reference standard (Dice scores 0.76/0.86 versus 0.61/0.55 for the two readers). V_{HI} measurements produced by the semiautomated workflow showed similar or better inter-observer agreement than visual scoring (based on Bland-Altman limits-of-agreement analysis), and provided similar response assessments.

Data Conclusion: V_{HI} measurements provide a precise assessment of inflammation with superior performance to visual assessment by trained expert radiologists. The proposed radiology-compatible workflow for V_{HI} measurement offers a mechanism to improve the consistency of radiological assessment of inflammation, and a biomarker of inflammation load in spondyloarthritis.

Keywords

Magnetic Resonance Imaging, Computer-Assisted Imaging Processing, Radiology

1 Introduction

Short inversion time inversion recovery (STIR) MRI is the workhorse of clinical imaging protocols for numerous inflammatory diseases, and shows areas of inflammation as increased signal. For example, in spondyloarthritis, areas of hyperintense signal in the subchondral bone are referred to as bone marrow oedema (BMO) and form part of the diagnostic criteria in this disease (1). However, despite the important role that STIR MRI plays in diagnosis and monitoring of inflammation, it is typically interpreted in a purely qualitative fashion. This introduces a source of subjectivity and consequently evaluation of inflammation burden can vary widely depending on reader expertise and the clinical setting.

The size of the problem was highlighted by a 2017 survey of 269 radiologists, which found wide variation in the use of MRI for assessing spondyloarthritis, including imaging sequences, anatomical coverage and image interpretation (2). Only 75% of radiologists reported awareness of spondyloarthritis as a disease entity, whilst only 25-31% were aware of formal MRI definitions of inflammation (2). Even in a controlled research setting, there is wide disparity in readers' agreement on the presence and severity of inflammation (3–6). This inconsistency creates a major risk of misinterpretation/misdiagnosis and inappropriate treatment. In clinical trials, it contributes to reduced power/increased sample size and increased cost.

In addition to the difficulties with interpretation, clinical radiological reports in spondyloarthritis are descriptive without quantitative assessment of inflammation. This introduces scope for misunderstanding of the report, particularly when styles differ between radiologists (7). A quantitative, easily-understandable biomarker of inflammation could potentially simplify interpretation substantially for the recipients of these reports.

To address the need for more objective inflammation assessment, here we develop a deep learning-enabled segmentation workflow aiming to combine the benefits of automated segmentation with those of human control and oversight of the assessment process. The final segmentation from this semiautomated workflow defines the volume of hyperintense inflammation (V_{HI}), which we propose as a quantitative imaging biomarker of inflammation load. We hypothesise that this biomarker can provide an accurate, precise and responsive method of scoring inflammation for use in clinical practice.

2 Methods

2.1 Overview of study design

We aimed to develop a partially-automated deep learning-based segmentation workflow for measuring the volume of hyperintense inflammation (V_{HI}), which is proposed as a quantitative imaging biomarker of inflammation load. To do this, we implemented and evaluated this workflow in a prospectively-acquired dataset. To assess the performance of V_{HI} as a biomarker, we assessed its relationship with visual scoring, inter-observer agreement and responsiveness to biologic therapy in patients with spondyloarthritis who underwent scans before and after biologic therapy. The data, code and models used in the study are available at (*anonymised*).

2.2 Study cohort

Data were taken from a completed prospective longitudinal study conducted at (*anonymised*) hospital between April 2018 and July 2019 (29 subjects consisting of 13 males, 16 females; mean age 42.4 years) with the aim of evaluating the ability of quantitative imaging biomarkers to measure and predict response to biologic therapy and performed with institutional review board approval (*anonymised IRB reference code*).

Potential participants were identified from clinical records of patients due to start biologic therapy and were initially approached about participation by rheumatologists at UCLH. Patients were included in the study if they were aged 18 to 85 years with a diagnosis of axial spondyloarthritis according to 2009 ASAS criteria (8) and active disease according to the National Institute of Clinical Excellence (NICE guidelines NG65) criteria. Exclusion criteria included contraindications to MRI such as metallic implants, pacemaker, severe claustrophobia, pregnancy, body weight > 150kg, treatment with an oral, intra-articular or intra-muscular glucocorticoid within 4 weeks. All patients underwent MRI scan of the sacroiliac joints, and continued in the study if their MRI fulfilled ASAS criteria for sacroiliitis(9) and were eligible for their first biologic drug (biologic naive) or a change biologic therapy (switchers) in accordance with best practice (NICE guidelines NG65). A repeat scan was performed after 12 weeks (+/- 2 weeks) of continuous anti-TNF treatment or 16 weeks (+/- 2 weeks) of anti-IL 17 treatment. Patients were withdrawn from the study if biologic therapy was declined, contraindicated or stopped owing to adverse events.

2.3 Clinical assessments

Information regarding patient demographics (age, sex and ethnicity), disease duration, history of peripheral arthritis and enthesitis, extra-articular manifestations, human leucocyte antigen (HLA) B27 status, drug history and smoking history were recorded at baseline. BASDAI and ASDAS scores as well as CRP and ESR were recorded at baseline and after 12-16 weeks of continuous treatment. A clinical response was assessed on the basis of a BASDAI improvement of ≥ 1.2 and an improvement in spinal VAS of ≥ 1 . This criterion is in accordance with NICE criteria and was chosen to reflect real-world clinical practice in the UK. Other clinical response measures included a reduction in BASDAI by 50% (BASDAI 50), a clinically important improvement in ASDAS (CII ASDAS) defined as a change in ASDAS >1.1 and inactive disease defined as an ASDAS of < 1.3 (ASDAS ID).

2.4 Image acquisition

Images were acquired on a 3T Philips Ingenia scanner. Both conventional and quantitative MRI scans were acquired for the study. Here, we focused on the conventional MRI protocol data to ensure wide applicability, although the workflow is general and could also be applied to quantitative MRI data. The conventional MRI protocol consisted of STIR and T1-weighted turbo spin echo sequences acquired in an oblique coronal plane (parallel to the sacrum) with fixed field of view. Quantitative MRI sequences, consisting of Dixon and diffusion-weighted MRI, were also used but not analysed for the present study. For the STIR acquisition, parameters included: TR 5316ms, TE 50ms, TI 210ms, echo train length 21, slice thickness 3mm, pixel spacing 0.59x0.59mm, image matrix 336x336, number of slices 23-25. All data were anonymised prior to export from the scanner and subjects were given unique study identifiers for data handling.

2.5 Deep learning-enabled segmentation workflow

2.5.1 Workflow overview

Inflammation was segmented using a semiautomated workflow incorporating deep learning as well as human interpretation; a schematic illustration is shown in Figure 1. Rather than training a neural network on areas of disease, the network is simply trained to recognize potentially-inflamed areas of bone, which are referred to as 'disease regions', and then a threshold is used within these disease regions to segment inflammation. This approach has

the advantages that (i) training a network to detect potentially-inflamed regions (rather than direct recognition of pathology) is a simple task which can be achieved with a relatively small dataset, (ii) the disease-region segmentations can easily be propagated onto images from other sequences (provided they were acquired with the same FOV), thus enabling assessment of disease with multiple sequences if desired, and (iii) the final threshold-based segmentation step is transparent and easily-understood.

The pipeline comprises the following steps:

(i) *'Normal bone region' segmentation*

Normal bone marrow in the interforaminal region of the sacrum (which is typically spared from inflammation) is segmented, using STIR images. Here, we performed this step manually to ensure that any artifacts or vessels were avoided, although this step can be straightforwardly automated using deep learning.

(ii) *Estimation of STIR intensity threshold*

The normal bone segmented in (i) is used to select a threshold towards the upper end of the normal bone intensity distribution, enabling separation of normal from inflamed marrow within the disease region (described below).

(iii) *'Disease region' segmentation*

Areas of potential inflammation (all of the imaged bone in the pelvis, including bone adjacent to the SIJs, apart from the normal bone region) are segmented on T1W images using a supervised convolutional neural network with U-net architecture (10).

(iv) *Thresholding within the disease region*

Voxels in the disease region are assigned labels of 0 if voxel intensity is below the intensity threshold and 1 if above the intensity threshold

(v) *Automatic removal of very small segmented regions*

Regions containing <4 pixels (i.e. any region with an area <1.39mm²), which are commonly due to noise or small vessels within the bone marrow, are automatically removed.

(vi) *Manual correction of the final segmentation by a human observer*

Correction is based on morphology and anatomical location. Once the correction procedure is complete, the final corrected segmentation defines the volume of STIR-hyperintense inflammation (V_{HI}), which is the proposed biomarker of inflammation load. V_{HI} can be defined in terms of the volume *per se* (e.g. in mm^3) or as a voxel count (the former is simply the voxel count multiplied by the volume of an individual voxel).

2.5.2 Details of Step (ii) – Determining the segmentation threshold from the ‘normal bone region’

Two different thresholds were obtained from the distribution of intensity values in the normal bone region, in order to provide one ‘conservative’ and one ‘sensitive’ segmentation. To provide the ‘conservative’ segmentation, an upper limit, L_{upper} was defined as the maximum intensity, I_{max} of the distribution. To provide the ‘sensitive’ segmentation, a lower limit, L_{lower} was computed as the sum of the upper quartile, Q_U and a multiple, n of the inter-quartile range, IQR of the distribution $L_{\text{lower}} = Q_U + n \cdot IQR$. The multiple was determined automatically in order to adapt the ‘sensitivity’ for each scan for each patient: starting with the value of 1.5, the multiple n was incremented by 0.05 until the difference between upper and lower limits was less than the half of the interquartile range, $0 < L_{\text{upper}} - L_{\text{lower}} < IQR/2$. If the condition was initially satisfied, no incrementation was performed. Note that, for the primary analyses in this study, we used the lower, ‘sensitive’ threshold to determine V_{HI} .

2.5.3 Details of Step (iii) – Disease region segmentation

Step (iii), i.e. the disease region segmentation, employed a convolutional neural network with 2D U-net architecture. To enable an assessment of generalisability, the network was first trained and tested on a subset of the full dataset (consisting of 248 T1W image slices from 10 subjects), before a further evaluation of segmentation performance was performed by qualitative visual assessment on the remaining 19 subjects.

Reference standard

The reference standard for training was manual segmentation of the disease region, including all bone in the imaged pelvis, the sacroiliac and facet joint spaces (Figure 2). The segmentation was performed by a postdoctoral researcher with two years of MRI

experience who had received training in interpretation of the relevant anatomy by a radiologist; this radiologist also performed a slice-by-slice review of the segmentations in a subset of the cases to ensure that these anatomical assessments were accurate.

Segmentations were performed using ITK-SNAP Version 3.8 (11).

Data partition

Data was first partitioned at subject level at random into two sets: 200 image slices (8 subjects) for training with four-fold cross validation to find the optimal set of hyper-parameters and 48 image slices (2 subjects) for testing. The first set was then subdivided four times (for each of the four validation folds) into a training subset (150 image slices, 6 subjects) and validation subset (50 image slices, 2 subjects); this subdivision was performed at subject level to avoid any 'contamination' of the test dataset as a result of similarity individual subjects' image slices.

Data pre-processing and augmentation

To allow the same intensity scale between subjects and consistency in intensity levels of voxels representing the same tissue for each subject, images were normalized by three standard deviations of the image intensity distribution. Each pre-processed image (and the corresponding segmentation masks from the reference standard) underwent elastic deformation (<https://github.com/gvtulder/elasticdeform/tree/v0.4.9>), affine transformation (rotation, scaling, shearing) and random flip with 0.5 probability. To make the network robust against between-subject variations in the intensity level of bone voxels, intensities were raised to a random power after normalisation. All transformation parameters (rotation angle, scaling and shearing factors, power) were randomly sampled from uniform distributions of pre-defined ranges.

Model training

A convolutional neural network with two-dimensional U-Net architecture (10) was trained on mini-batches by optimizing binary cross entropy loss (12) using the Adam optimizer (13). A publicly-available implementation in Pytorch was used (<https://github.com/jvanvugt/pytorch-unet>). The architecture included batch normalization to keep the distribution of convolution layers outputs fixed, allowing faster convergence (14). The network was trained with pre-processed data augmented on the fly, which

allowed a substantial increase of the diversity in the training samples. At each training epoch 350 augmentation steps were performed (15). At each step, a random batch was selected from the available pool, augmented, and fed into the model. Data shuffling ensured that the same batch contained different image slices every epoch. Optimal hyper-parameters were identified through training with four-fold cross validation, specifically, (i) the number of epochs (60, 100), (ii) the number of resolution levels (2,4,6), where a level represents all feature maps between two max-pooling or two up-sampling operations (15) and (iii) convolution kernel size (3×3, 5×5). The batch size (four) and learning rate (0.001) were kept constant. The model parameters were initialized using the default Pytorch initialization scheme.

Once the optimal set of hyper-parameters was determined, the network was trained three times to reduce individual model's errors, using 200 image slices (8 subjects). Average prediction from three models was computed, then rounded, and performance of model averaging ensemble was evaluated.

Model evaluation

The performance of the model (averaging ensemble) for disease region segmentation was evaluated in two ways. First, to provide an evaluation in terms of the Dice coefficient (details in Supplementary information S1), performance was assessed against manual segmentation on the test dataset of two subjects (48 slices). Second, to assess the generalisability on the model on a variety of clinical cases, a further evaluation was performed by visual assessment (either satisfactory or not satisfactory) on a further 19 subjects (38 scans, 950 image slices), for which manual segmentations were not performed. Note that, to make use of all the available annotated data the model was re-trained three times using all 10 subjects, i.e. 248 slices, prior to the evaluation on the further 19 subjects. The visual assessment was performed by a postdoctoral researcher with two years of MRI experience who had received training in interpretation of the relevant anatomy by a radiologist; this radiologist also performed a slice-by-slice review of the segmentations in a subset of the cases to ensure that these anatomical assessments were accurate.

For the purposes of the subsequent assessment of the performance of the *complete workflow*, disease region segmentations (manual and automated) from 29 subjects were

used. If the automated segmentation failed, the segmentations were manually corrected for use in the subsequent evaluation.

2.5.4 Details of Step (vi) – ‘Cleaning’

The manual correction (‘cleaning’) procedure in Step vi was performed by two consultant radiologists, with over 25 and 7 years of musculoskeletal MRI experience respectively, as follows. Regions which were deemed non-inflammatory – for example due to the presence of vessels or artefact – were removed by readers based on morphology and anatomical location.

To minimise subjectivity, lesions were either left in place or removed altogether, i.e., the boundaries of lesions were not modified, except when the posterior part of the joint or foramen were segmented along with a potential lesion. To facilitate the comparison with visual scoring of bone marrow oedema (see details in the following section), areas of inflammation located above the L4/5 disc and within the sacroiliac joint space were removed by the observers as part of the cleaning process, meaning that the cleaned segmentations contained only subchondral bone marrow oedema.

T₁-weighted images were used to assist readers in identification of anatomical structures and regions of increased fat content. The two readers discussed and agreed upon the procedure prior to manual correction.

2.6 Conventional visual scoring

To provide a comparator to V_{HI} , visual scoring was performed on the same STIR images as those used for the semiautomatic segmentation using the SPARCC BME system (16), by the same two consultant radiologists as performed the cleaning procedure. Images were read in random order on a dedicated research workstation where the reader was blinded to clinical diagnosis, treatment and all quantitative measurements, including V_{HI} . The presence of bone marrow oedema (BME) was evaluated in six consecutive slices, with the SIJs divided into eight quadrants. Each quadrant was scored for the presence/absence of BME (1 or 0) with an additional score of 1 if the BME in a quadrant was more than 10mm deep and a further additional score if the BME was at least as intense as the cerebrospinal fluid. A total score out of 72 was reached for SPARCC BME.

2.7 Performance Assessment

2.7.1 Comparison of inter-observer segmentation overlap - semiautomated pipeline versus purely manual segmentation

To characterise the variability in manual segmentation and to establish a baseline segmentation performance, both radiologists performed two sets of purely manual segmentations in a subset of eight patients. This design allowed separation of the effects of inter- and intra-observer variability on segmentation performance, and meant that poor performance due to differences in opinion/expertise could be distinguished from intrinsic difficulties with performing the task consistently. The segmentations were temporally separated by one month to minimise any learning effect, and the eight subjects were selected to provide a range of inflammation severities. Having established the performance baseline, inflammation was again segmented in the same eight subjects by the same radiologists using the semiautomated workflow.

Inter-observer was compared between the semiautomated and purely manual segmentations in terms of Dice scores (further detail is provided in Supplementary Information S1). To provide a further evaluation in terms of accuracy, we constructed a composite reference standard using a majority vote from both methods. Voxels which were deemed inflamed at least three times from two manual segmentation trials and two semiautomated segmentation trials were taken to be truly inflamed. The performance of the two methods was compared against this composite reference standard in terms of Dice scores.

2.7.2 Comparison of interobserver agreement - V_{HI} versus visual scoring

Before proceeding to the agreement analysis, the relationship between V_{HI} scores and visual scores was analysed graphically using scatterplots. To improve visualization of V_{HI} measurements clustered at the lower end of the range, scatterplots were generated with the raw data and also following (i) data truncation to remove the highest V_{HI} values and (ii) $\log(x+1)$ transformation to linearize the relationship between V_{HI} and visual scores whilst ensuring that 0 values are unaltered after transformation (for ease of interpretation). The relationship between V_{HI} and visual scores was evaluated with linear regression; slope and intercept values were reported with 95% confidence intervals.

Bland-Altman 95% limits of agreement (LoA) analysis was performed for both V_{HI} and SPARCC scoring. Plots were generated using raw data, truncated data and $\log(x+1)$ -transformed data across the full dataset of 29 patients. The mean bias and 95% LoA were calculated and reported using the raw, non-transformed data for both V_{HI} and visual scores. For the purposes of this analysis, only inflammation present in the subchondral bone was included in the final cleaned segmentations, in order to facilitate a more direct comparison with SPARCC scoring (which includes only subchondral bone marrow oedema).

2.7.3 Responsiveness to biologic therapy - V_{HI} versus visual scoring

Changes in V_{HI} and visual scores after treatment were visualized using spaghetti plots in which changes in both measurements for individual patients were depicted. Separate plots were generated for those patients who showed evidence of response to therapy using clinical criteria and for those patients who did not. To provide a numerical summary of the ability of V_{HI} to capture response, we recorded the agreement between clinical response assessment and V_{HI} -based response assessment and between clinical response assessment and SPARCC-based response assessment. For the purposes of this analysis, any patient undergoing an improvement in V_{HI} /SPARCC was deemed to be a V_{HI} /SPARCC responder. Note that this is an imperfect assessment and an alternative would be to have a threshold for response based on the variance in the data, however, the latter is problematic when the distributions of the data are so different for V_{HI} and SPARCC and risks creating an unfair threshold depending on the specific transformation used. The proposed approach, whereby any improvement is regarded as a response, is not regarded as a clinically meaningful threshold but rather as a useful simplification for the purpose of this analysis.

2.7.4 Failure Analysis

Error analysis was performed for any scan in which the difference in V_{HI} between observers was more than two standard deviations from 0. Specifically, the scans and accompanying segmentation masks for each 'error case' were inspected to determine the reasons for discrepancy; errors were classified as anatomical (relating to whether hyperintense regions classified as subchondral or not), morphological (relating to whether hyperintense regions were classified as oedema rather than vessels) or artifact-related (relating to whether hyperintense regions were deemed artefactual).

3 Results

3.1 Overview

An example of normal bone segmentation is shown in Figure 1b, an example of disease region segmentation is shown in Figures 1c and 2, and an example of inflammation segmentation (without the final cleaning step) is shown in Figures 1e and 3. The final cleaning step is highlighted in Figure 1f. The following subsections describe specific evaluations of the individual components of the workflow, and of the performance of the workflow as a whole for inflammation assessment.

3.2 Disease region segmentation performance

The model was successfully trained without evidence of overfitting. The learning curves for the training procedure (for different training subsets and validation folds) are shown in Supplementary Figure S2.

Assessing performance in terms of Dice scores (test dataset of 48 slices from two subjects), the model ensemble yielded a mean (range) Dice of 0.94 (0.85 to 0.98), indicating excellent segmentation performance. Examples of automatically segmented disease regions in the test dataset and the corresponding reference standard segmentations are shown in Figure 2.

Assessing performance qualitatively (19 further subjects), model performance was either perfect or subject to minor corrections for 16 subjects. The model failed in three subjects, each of whom was found to have abnormal bone marrow (high fat content or extensive sclerosis, which were not present in the training dataset). Examples of model failures are shown in Supplementary Figure S3.

3.3 Comparison of inter-observer segmentation overlap - semiautomated pipeline versus purely manual segmentation

The improvement in segmentation performance provided by the workflow is shown in terms of Dice scores in Figure 4.

For purely manual segmentation (without the workflow), Dice scores from the two observers' segmentation volumes ranged from 0.28 to 0.87. Intra- and inter-reader median Dice values were 0.63 and 0.69 for reader 1 and 2 and in the range 0.53-0.56, respectively.

The median Dice scores improved to 0.84 using the workflow, representing an increase of 28-31% compared to pure manual segmentation.

Against the composite reference standard, Dice scores were substantially higher for the semiautomated method (median Dice 0.76 and 0.86 for the two readers) than for the manual segmentation method (median Dice 0.61 and 0.55) (Figure 5).

There was one outlier where the agreement was reduced for the semiautomated method; review of the images indicated that the disagreement mostly related to the presence of inflammation in the joint space, where blood vessels can be misinterpreted.

3.4 Comparison of interobserver agreement - V_{HI} versus visual scoring

The relationship between V_{HI} and visual scoring is shown in Figure 6. Note that V_{HI} shows a nonlinear relationship with SPARCC scoring, reflecting the fact that SPARCC scoring gives binary scores for each quadrant and therefore effectively ‘plateaus’ at higher inflammation volumes. The relationship becomes approximately linear with logarithmic transformation.

Bland-Altman limits-of-agreement plots for V_{HI} and visual SPARCC scoring are shown in Figure 7. The Bland-Altman LoA were +191 (-4119 to 4501) voxels over a range of 9.5 to 90081 for V_{HI} and -1.5 (-14.8 to 11.8) voxels over a range of 0 to 47.5 for SPARCC scoring. Note that the limits are narrower for V_{HI} than visual scoring relative to the range of mean values in the data, suggesting improved inter-observer agreement.

After logarithmic transformation, the widths of the LoA were similar for V_{HI} and visual scoring relative to the range of values in the data, suggesting similar inter-observer agreement. However, note that the log-transformed data highlights greater disagreement in cases where the clinical burden of inflammation is small. This is natural because decisions on the presence / absence of inflammation are more difficult when only small regions are involved. Furthermore, note that the difference in log-transformed scores indicates proportional disagreement, which can be large even when the absolute size of the differences is small.

3.5 Responsiveness to biologic therapy - V_{HI} versus visual scoring

Examples of pre- and post-treatment scans and accompanying segmentations for a single subject are shown in Figure 8, and response plots are shown in Figure 9.

16/29 patients underwent a clinical response. Of the 16 clinical responders, 11/16 were also classified as responding by V_{HI} and 12/16 were classified as responding by SPARCC scoring. Of the clinical non-responders (13/29), 4/13 were also classified as non-responding by V_{HI} and 6/12 were classified as non-responding by SPARCC scoring.

V_{HI} and clinical assessment agreed on response/non-response in 15/29 subjects. SPARCC scores and clinical assessment agreed on response/non-response in 18/29 subjects. SPARCC scores and V_{HI} agreed on response/non-response in 19/29 subjects.

There was a significant linear relationship between the change in V_{HI} and the change in SPARCC scores, with an estimated regression slope (95% CI) of 2408 (1230 to 3586) ($P=0.0003$) and an estimated intercept of 894 (-10760 to 12547) ($P=0.88$).

3.6 Failure Analysis

Discrepancies between the two observers for the semiautomated segmentation were identified in 3/58 cases. The images from these cases are shown in Supplementary information S4. Inspection of these images revealed that disagreement was 'anatomical' in all two cases (i.e. relating to the location of hyperintensity) and 'artefactual' (i.e. relating to whether hyperintense regions were deemed artefactual) in one case; there were no instances of morphological (e.g. relating to whether hyperintense regions were classified as oedema rather than vessels) disagreement. Specifically, in the two cases of 'anatomical' disagreement, the observers disagreed due to the presence of hyperintense bone in the posterior ilium, which was attributed to inflammation by one observer but to anatomical variation by the other. In the one case of 'artefactual' disagreement, there was diffuse and mild hyperintensity in subchondral bone which was deemed inflammatory by one reader but normal by the other; this was a post-treatment scan in a patient with extensive inflammation that had improved after treatment – i.e. the difficulty in this case related to the identification of resolving inflammation.

4 Discussion

At present, there is no imaging biomarker of inflammation that is used widely in clinical practice, and image interpretation is performed in a qualitative fashion, introducing substantial subjectivity. Here, we propose a quantitative imaging biomarker known as the volume of hyperintense inflammation - V_{HI} – which provides similar information to SPARCC scoring (which is confined to the research setting) and avoids the need for subjective and laborious visual assessment of image intensity. V_{HI} measurements should be simpler to interpret for clinicians than qualitative reports, and the accompanying segmentations provide a visual illustration of disease burden which is easy to understand for clinicians and patients. By first using a U-net - the current state-of-the-art approach for medical image segmentation (10,17) - to recognize potentially inflamed bone and then segmenting areas within this using thresholding, our approach has the advantages that (i) the disease region segmentation is relatively trivial and can be achieved with a relatively small dataset, (ii) these segmentations can easily be propagated onto images from other sequences, and could easily be applied to quantitative MRI, and (iii) the segmentation of inflammation is transparent, easily-understood and objective, removing the need for subjective intensity-based judgements to be made by radiologists. Furthermore, the semiautomated nature of the workflow means that the burden placed on the radiologist is minimised (since cleaning is a simple and relatively straightforward process relying only on the identification of artifacts), making it amenable to use within a standard radiological workflow. Our approach is broadly similar to how semiautomated segmentation is already used for techniques such as coronary calcium scoring (18,19).

The key results of our study are as follows. Firstly, the semiautomated workflow produced a marked improvement in inflammation segmentation performance compared to the purely manual approach, both in terms of inter-observer agreement and against a composite reference standard. Second, V_{HI} measurements show similar or better inter-observer agreement than visual scoring, although direct comparison is difficult due to the differences in the metrics' distributions: comparison on the non-transformed data suggests superior performance for V_{HI} and comparison on the transformed data suggests similar performance. The former may be more representative of performance in clinical practice, where absolute differences are more relevant than proportional differences. Thirdly, V_{HI} measurements

show a nonlinear, approximately exponential relationship with visual scoring, which becomes approximately linear with logarithmic transformation. This result may reflect the fact that V_{HI} can capture the full burden of inflammation present in the subchondral bone whereas visual scoring is limited to binary assessments for each quadrant of the joint, and thus does not distinguish between areas of inflammation of different sizes within a quadrant. From a clinical perspective, a technique with a greater dynamic range may be able to better stratify patients by inflammation burden and better capture changes in inflammation severity with treatment, even when inflammation does not completely resolve (for example, when performing early response assessments). Fourthly, V_{HI} and visual scoring provide broadly similar response assessments, although neither metric agrees closely with clinical response assessments. The latter point probably reflects the complex, multifactorial nature of pain and the fact that this is not solely due to inflammation.

Several previous studies have also investigated the use of threshold-based methods for quantifying inflammation (20,21). However, these studies relied on manual segmentation to identify an optimal threshold, whereas our data suggest that using manual segmentation as a “gold standard” is problematic and may lead to inconsistent interpretation especially in cases when inflammation is subtle or precise lesion boundary cannot be identified. To highlight this point, a recent study aiming to demonstrate the feasibility of fully-automated segmentation of BME (22) revised the threshold value developed in earlier work (20), finding an optimal threshold of 1 compared to 1.5 in the prior study. Clearly, a threshold which depends on reference standard provided by human observers is not desirable. In contrast, the approach proposed in this work removes the need for intensity-based judgements to be made by the observer. The use of an intensity-based threshold derived from normal marrow means that the choice of voxels is primarily influenced by the physical properties of the tissue, specifically, the extent to which the intensity in each voxel deviates from the intensity observed in normal marrow. The normal bone region effectively serves as a reference region and means that the judgment around which voxels are hyperintense is tailored to each individual and each scan.

Importantly, V_{HI} measurements should be simpler to interpret for clinicians than qualitative reports, which vary in style and length between radiologists and depend on expertise and opinion. The segmentation masks generated by the workflow could be displayed together

with the V_{HI} measurement, providing a visual illustration of disease burden which is easy to understand for clinicians and patients. Visual illustrations could make disease activity assessments easier to understand for patients and help them to feel more in control of their disease and care.

4.1 Limitations

A limitation of the study is that the network was trained on a relatively small dataset, and produced errors in cases which were atypical. However, the intention of this study is not to provide a definitive final algorithm, but to demonstrate the potential of the proposed deep-learning enabled workflow. The improvement in performance showed by our data suggests that further development, which might include network training on a larger, multisite dataset (thus introducing greater robustness to atypical cases), is warranted. Additionally, the performance of the method is fundamentally limited by the acquisition modality, which in this case was STIR imaging. Although widely used, STIR imaging has a number of limitations including its relatively poor signal-to-noise ratio and the potential for inadequate fat suppression. However, a strength of our approach is that it can easily be applied to other imaging modalities, including quantitative imaging, since the disease region masks can easily be propagated to other modalities. This is a substantial advantage comparing to requiring a network that is directly trained to identify inflammation on specific sequences. Finally, although the use of the semiautomated workflow improved agreement between observers, our results do indicate that subjective judgements made in the cleaning step of the workflow have a substantial impact on V_{HI} measurements. Further research could therefore focus on greater automation of the method, including automatic removal of vessels and image artefacts, further reducing subjectivity. However, retaining human control over the workflow may help radiologists to trust the workflow and therefore increase uptake in clinical practice.

4.2 Conclusion

V_{HI} measurements provide a precise assessment of inflammation with superior performance to visual scoring by trained expert radiologists. The proposed radiology-compatible workflow for V_{HI} measurement offers a mechanism to improve the consistency of radiological assessment of inflammation, and a biomarker of inflammation load to guide treatment decisions in spondyloarthritis.

5 Figures

Figure 1 – Schematic illustration of deep learning-enabled, semiautomated workflow.

A STIR image (outlined in green) and corresponding T1w image (outlined in red) (a) are used as the input. In this case, the STIR image shows left-sided sacroiliac joint inflammation.

The **normal bone region** is manually defined by a radiologist to determine the distribution of intensity values of normal bone (b). Manual segmentation is used for this step to enable the radiologist to exercise judgement over the most representative area of normal marrow. The **disease region** (region of potential inflammation) is automatically segmented by a convolutional neural network to determine areas of potential disease (c). The normal bone intensity distribution is determined from the normal bone, and two thresholds are defined [the maximum of the intensity distribution (upper threshold, red dotted line) and a multiple of the interquartile range (lower threshold, orange dotted line); a blue dotted line represents an empirical threshold value). Areas of tissue within the disease region above these thresholds are then denoted inflamed (e). Areas meeting the lower threshold alone are shown in yellow, whereas those meeting the upper threshold are shown in red. The final cleaning is performed by a radiologist to remove areas of artifact or inflammation outside the target area (f). In this example, areas of inflammation above the L5/S1 disc and in the sacroiliac joint space were removed (along with an artifactual lesion in the L5 vertebral body which was deemed to be due to a vessel) to facilitate a direct comparison with SPARCC visual scoring.

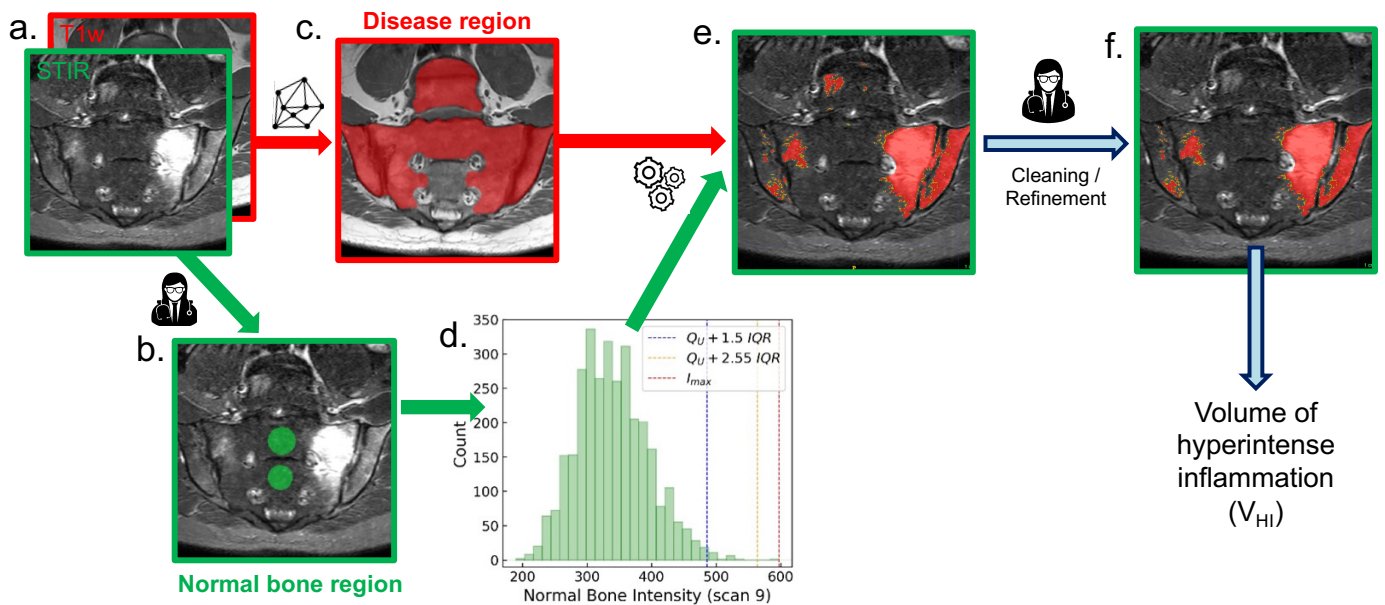


Figure 2: Automatic segmentation of disease region: demonstration of performance on examples from the test dataset. The T1w images (left-hand column), reference standard (middle column) and model averaging ensemble prediction of disease region (right-hand column) are shown for illustrative slices from two subjects (top and bottom row).

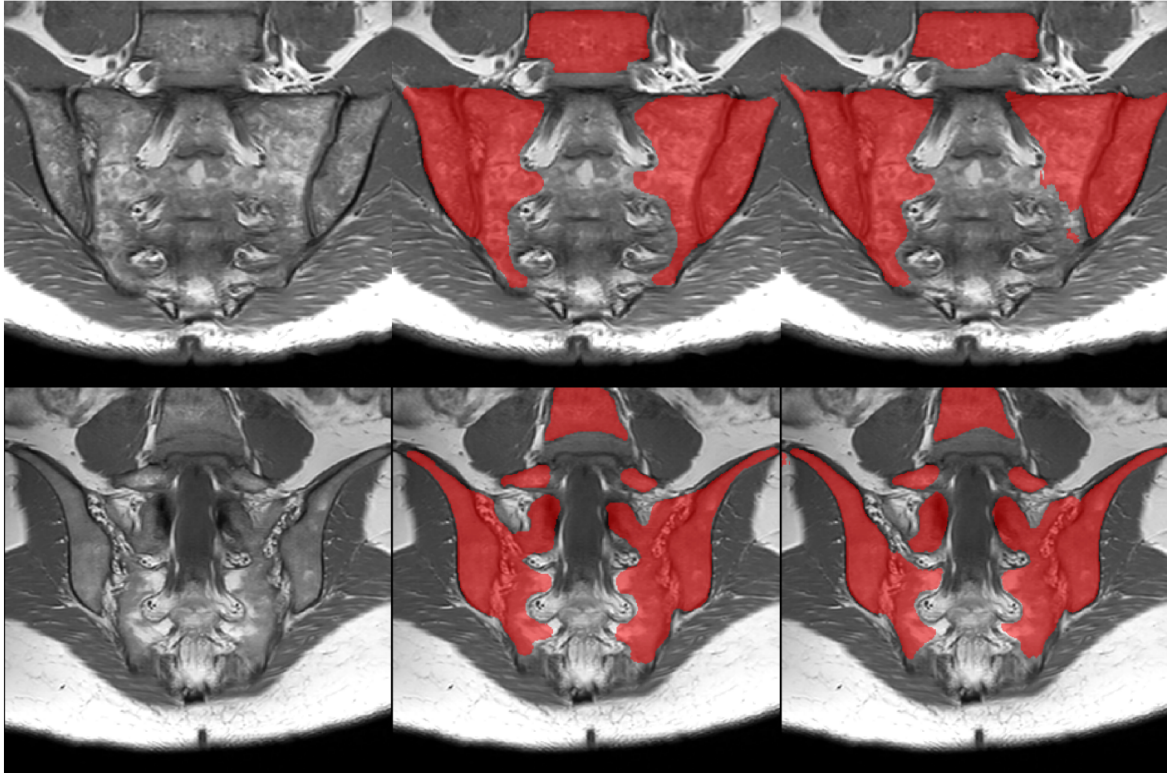


Figure 3 – Example outputs from workflow. Scans for two subjects are shown (S1 and S2, top and bottom row respectively). The left-hand column shows the STIR images, the middle column shows the preliminary segmentations (not cleaned to provide a demonstration of the performance of the automated component) and the right column shows visual summaries of the disease volume. Note that inflammation at the periphery of segmented lesions is typically captured by the lower ‘sensitive’ threshold, shown in yellow, whereas the most hyperintense inflammation in the centre of lesions is captured by the higher, ‘conservative’, threshold, shown in red.

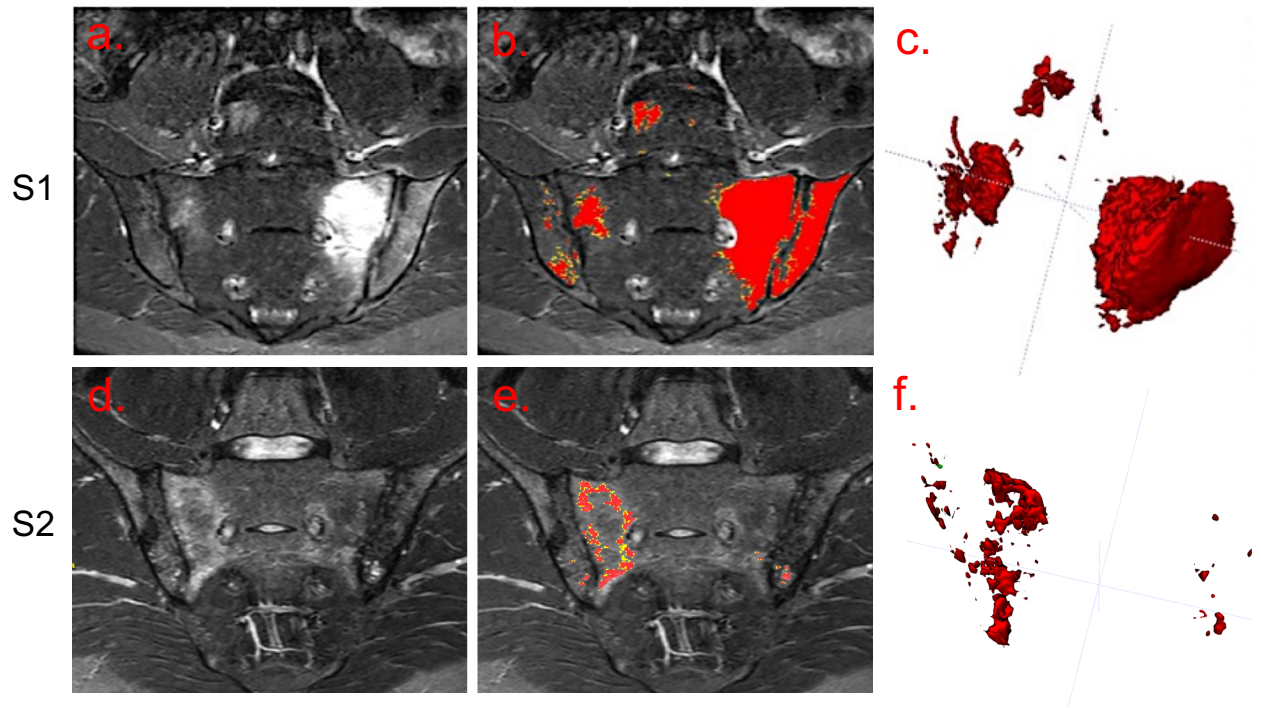


Figure 4 – Improvement in Dice scores for semiautomated procedure compared to purely manual segmentation. Dice scores are shown for individual patients for trials of segmentation of inflammation (volume comparison): (a) and (b) show results for purely manual segmentation and (c) shows results for corrected automatic (i.e. semiautomated) segmentations. (a) shows within-reader results, (b) shows between-reader-results and (c) shows between-reader results. R_{ij} stands for reader with the first subscript corresponding to the reader and the second to the segmentation trial. The figures show boxplots with individual datapoints superimposed; the red line represents the median dice.

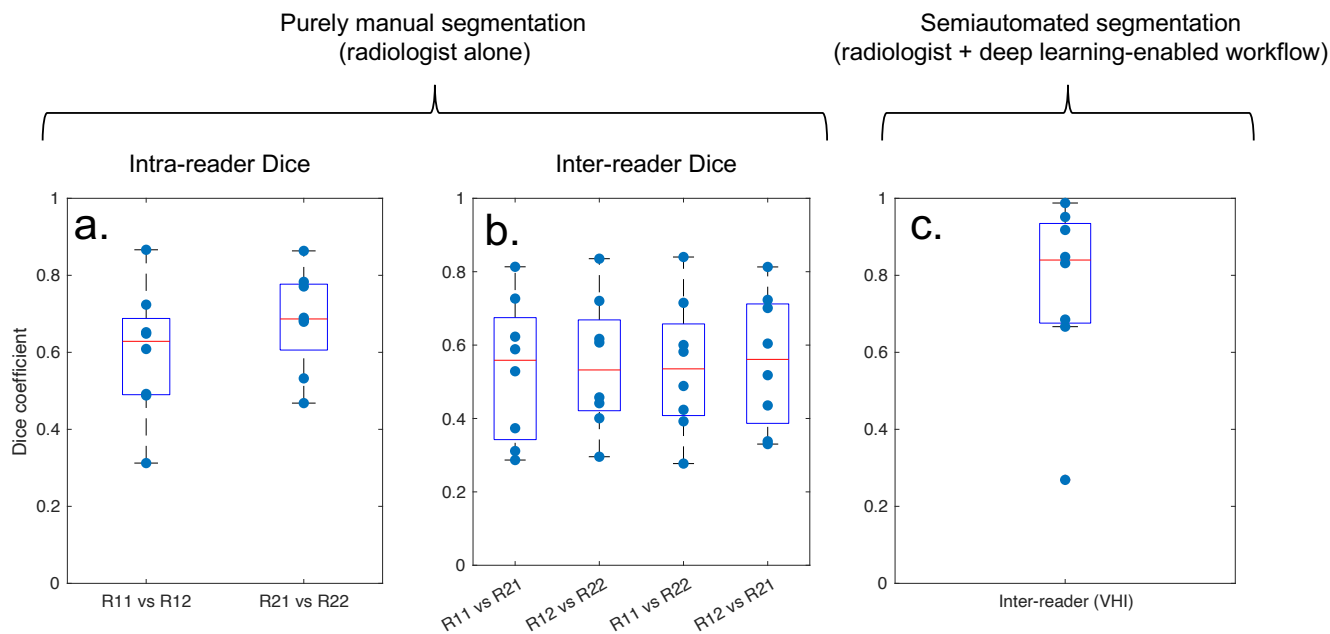


Figure 5 – Accuracy of semiautomated pipeline vs manual segmentation against a composite reference standard formed from both methods. The accuracy of the semiautomated method is substantially higher than that of the purely manual segmentation against the composite reference standard. The figures show boxplots with individual datapoints superimposed; the red line represents the median dice.

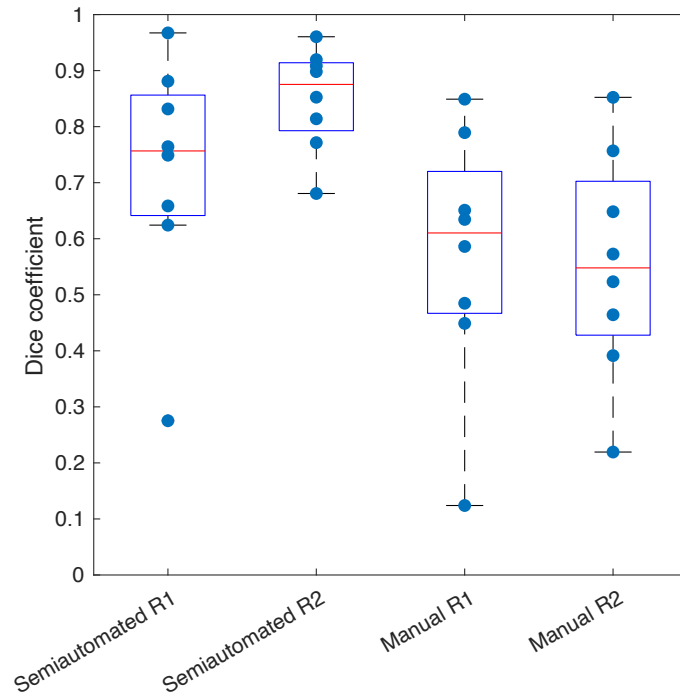


Figure 6 – Relationship between VHI and conventional visual scoring. The raw voxel counts (left column), voxel counts with truncation of the y-axis (middle column) and voxel counts with $\log(x+1)$ transformation (right-hand column) are shown on scatterplot. The truncation point used to generate (b) is shown on (a) as a blue dotted line. Note that the relationship between SPARCC scoring and inflammation volume is nonlinear but becomes approximately linear with $\log(x+1)$ transformation. Red points refer to pre-treatment scans, and blue points to post-treatment scans.

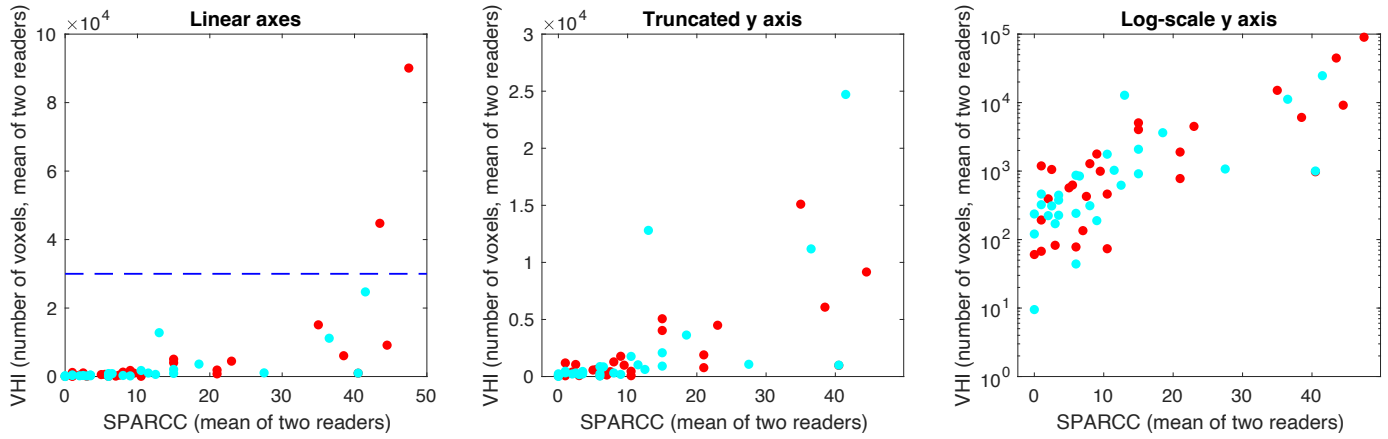


Figure 7 – Improvement in inter-observer agreement for V_{HI} . Bland-Altman plots for the two observers' scores are shown for VHI (top half) and SPARCC scores (bottom half). Red points refer to pre-treatment scans, and blue points to post-treatment scans. For VHI, the raw voxel counts (left column), voxel counts with truncation of the axes (middle column) and voxel counts with $\log(x+1)$ transformation (right-hand column) are shown on scatterplot (top row) and Bland-Altman plots (second row). The truncation points used to generate the middle column figures are shown as blue dotted lines on the plots in the left column. For SPARCC scores, the raw scores (left column) and $\log(x+1)$ transformed scores (right column) are shown on scatterplots (third row) and Bland-Altman plots (fourth row).

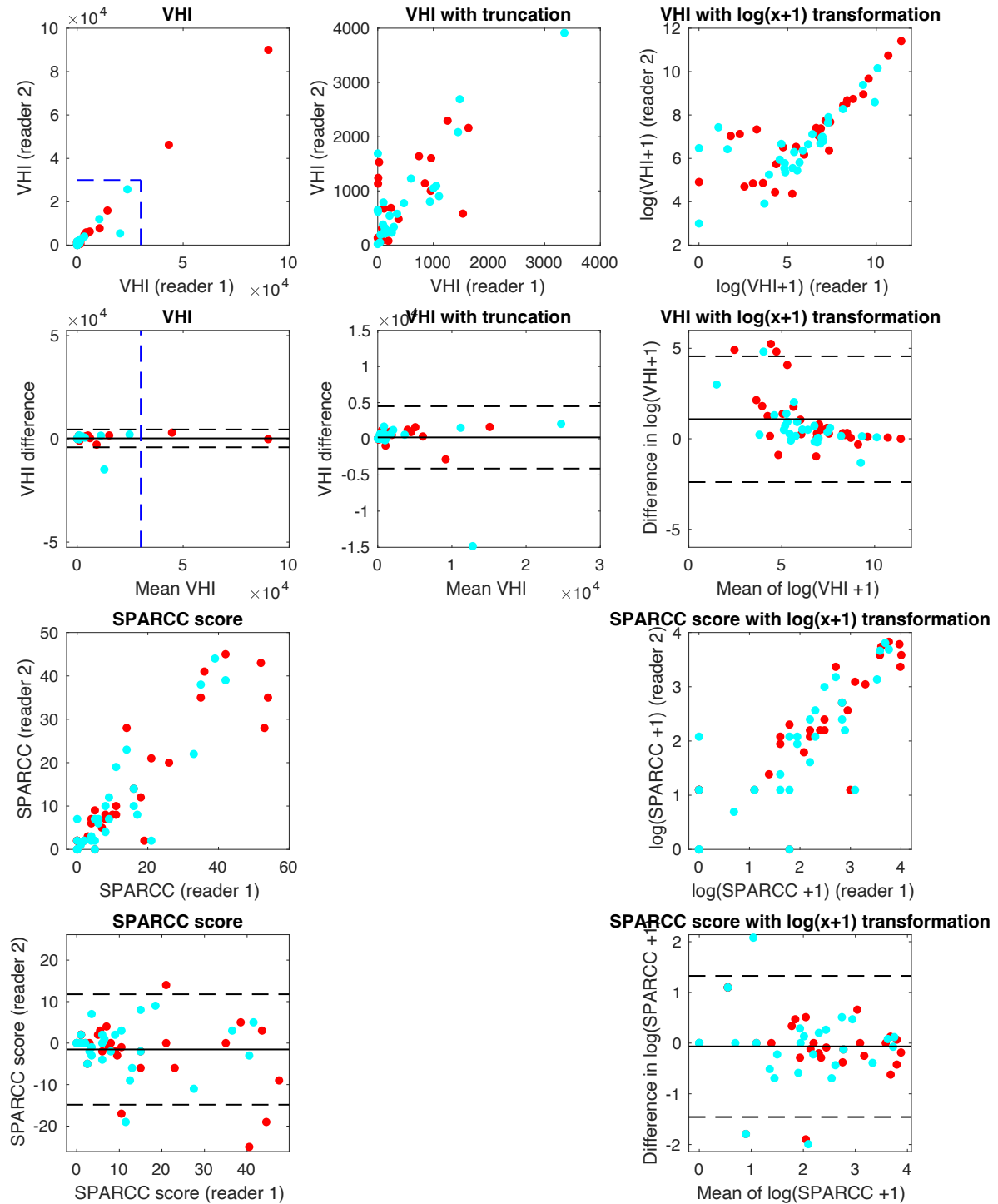


Figure 8 – Example of response to biologic therapy. Pre- and post-treatment scans for a single subject are shown (top and bottom row respectively). The left-hand column shows the STIR images, the middle column shows the preliminary segmentations (not cleaned to provide a demonstration of the performance of the automated component) and the right column shows visual summaries of the disease volume. Regions of acute inflammation showed a reduction in extent and intensity after treatment, although there is a persistent, slight hyperintensity compared to the normal interforaminal bone, which manifests as an increase in the proportion of inflammation captured by the lower (yellow) of the the two thresholds (see [Details of Step \(ii\) – Thresholding within disease regions](#)).

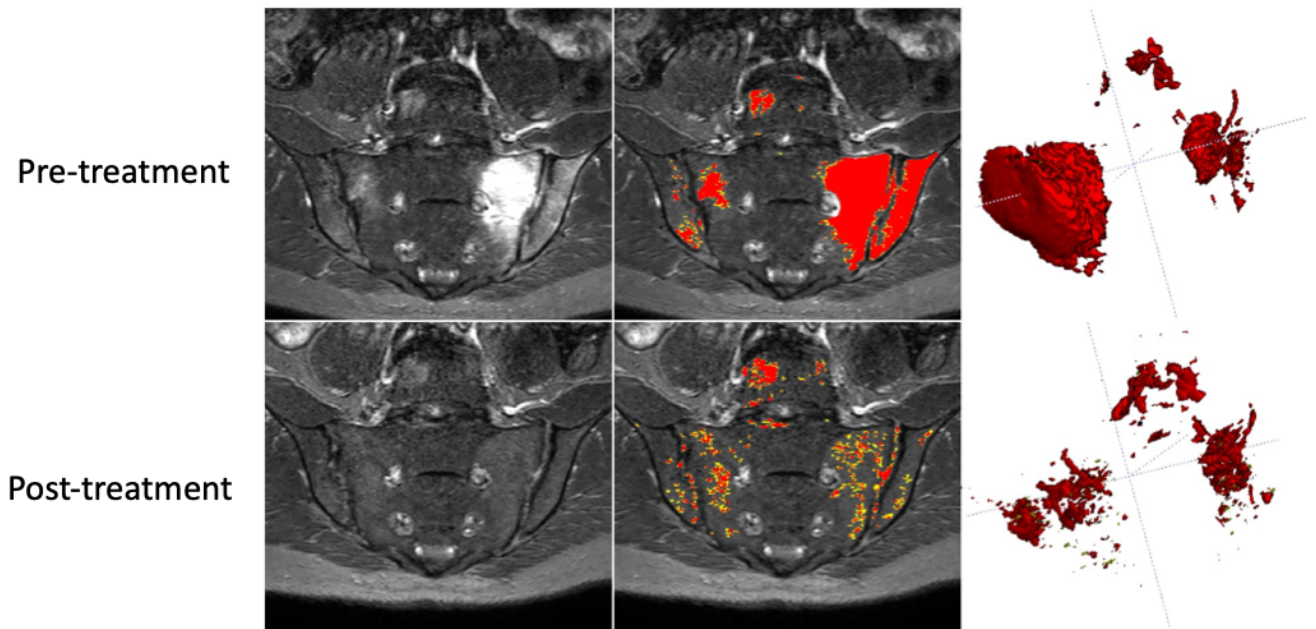
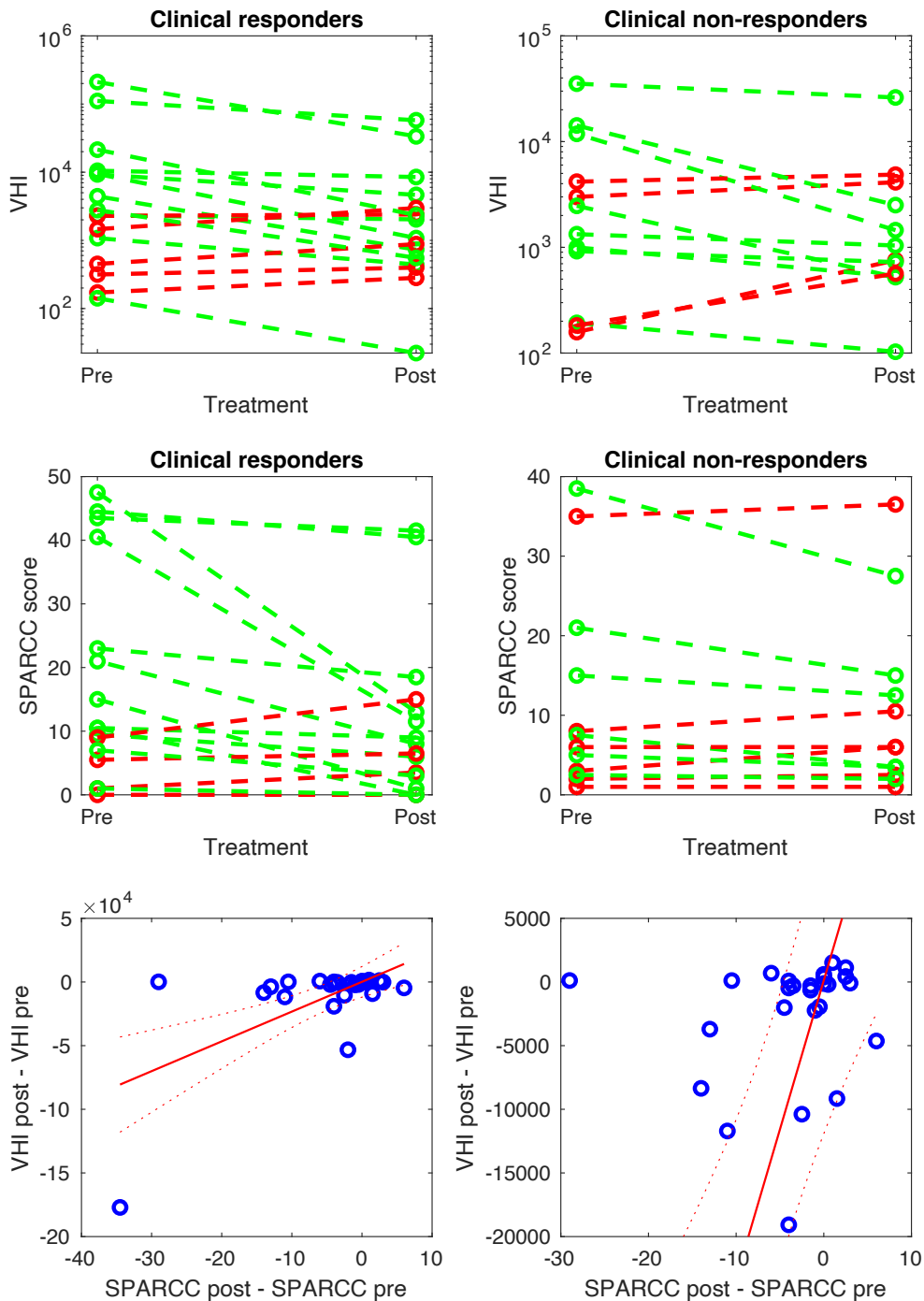


Figure 9 – Spaghetti plot for V_{HI} and SPARCC scores on pre- and post-treatment scans. Subjects with improving inflammation (based on imaging assessments by either V_{HI} or SPARCC score) are shown in green; subjects with worsening inflammation are shown in red. The first row shows results for V_{HI} and the second row shows results for SPARCC. The third row shows a scatterplot of V_{HI} changes against SPARCC changes for individual subjects, using the full data range (bottom left) and truncated y-axes (bottom right). The linear regression line has identical parameters for the two plots on the bottom row.



7 Supplementary Information

Supplementary Information S1: Evaluation Metrics

The similarity of a pair of binary segmentations was evaluated with the Dice coefficient, defined for the class of interest (abnormal or background) as the ratio of the number of pixels (voxels) having identical location in both segmentations to the average of number of pixels (voxels) in the segmentations [20]:

$$Dice = \frac{2|S_1 \cap S_2|}{|S_1| + |S_2|}$$

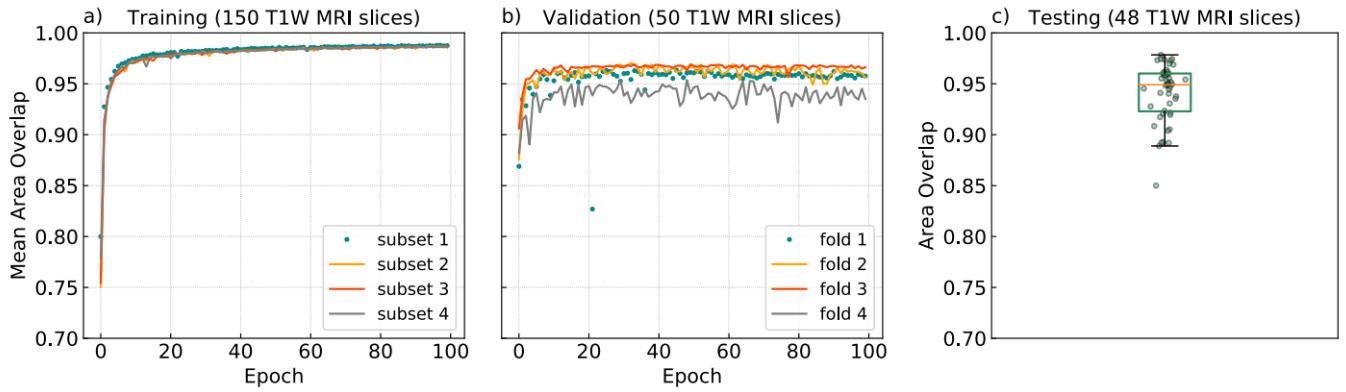
where $S_{i,i \in \{1,2\}}$ represents a point set, containing pixel (voxel) coordinates, the subscript i refers to the first or second segmentation and $S_1 \cap S_2$ is the intersection of the sets. We refer to the Dice coefficient as the *area* or *volume overlap*, depending on whether two segmented areas or volumes were compared.

To evaluate a deep learning model performance during training, a soft, differentiable generalization of Dice was used, implemented as [21]:

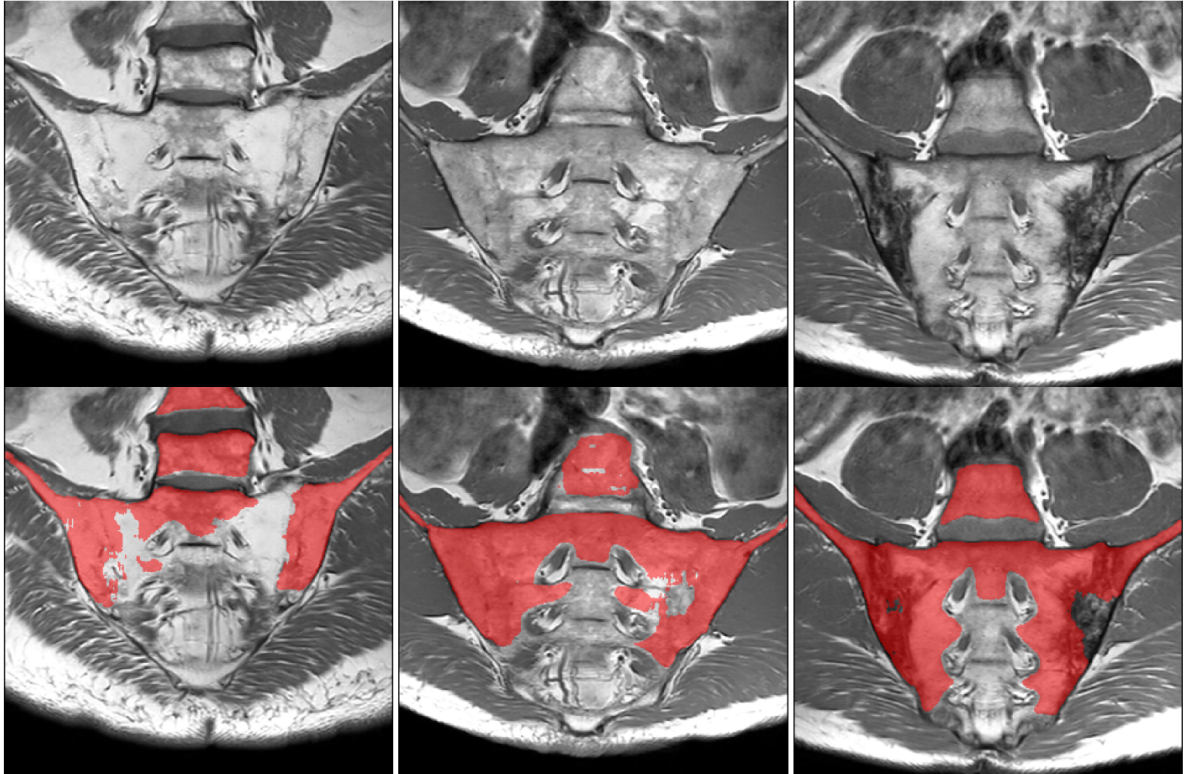
$$Dice = \frac{2 \sum_i^N r_i p_i}{\sum_i^N r_i^2 + \sum_i^N p_i^2}$$

where summation runs over pixels of reference standard, $r_i \in R$ and network probability map, $p_i \in P$.

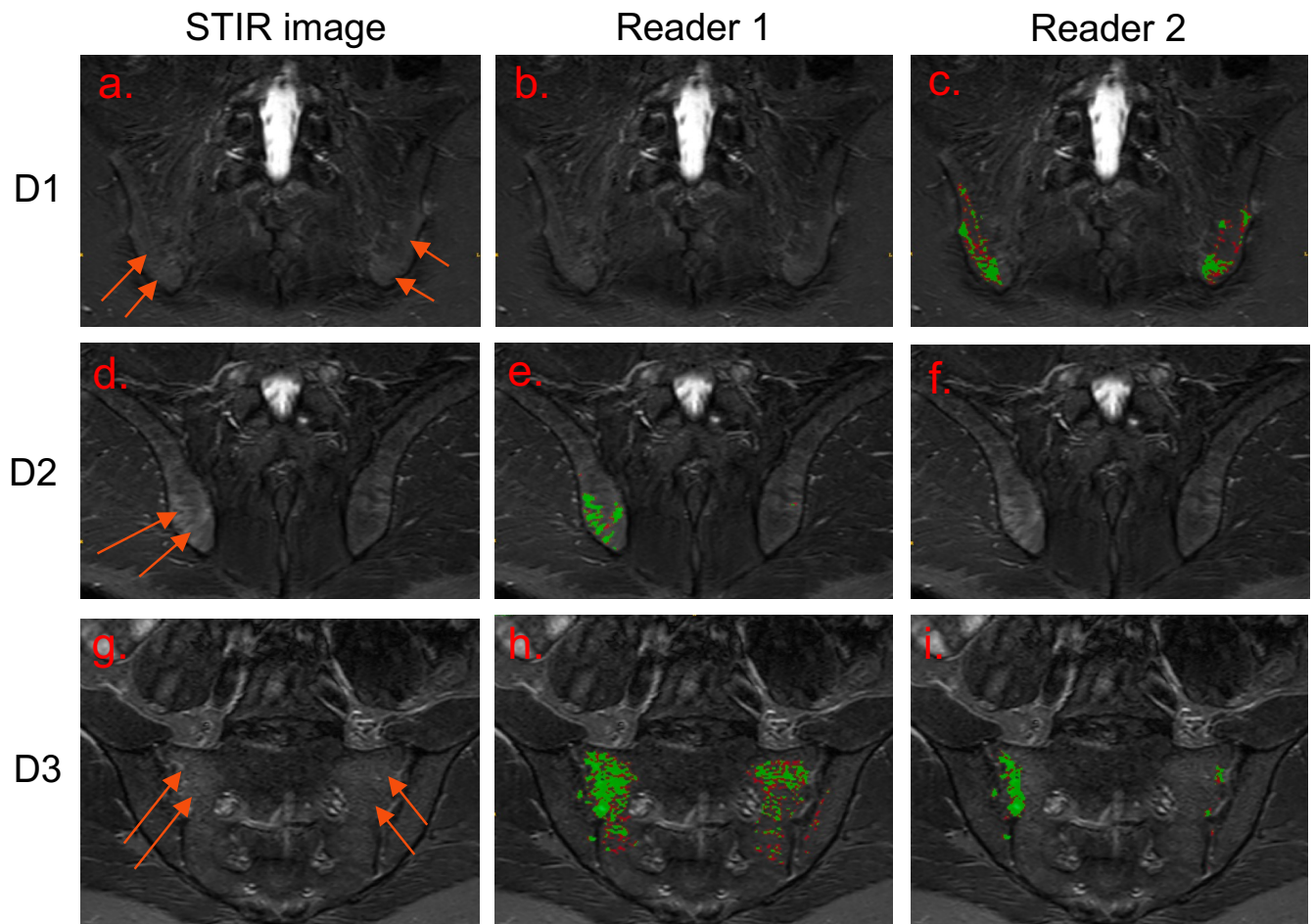
Supplementary figure S2 - Mean area overlap (Dice score) vs training epoch for different training data subsets (a) and validation folds (b). Each point represents Dice score averaged over (i) classes (foreground & background), (ii) samples in a mini batch and (iii) 350 augmentation steps. Area overlap from pair-wise comparison of reference standard and rounded prediction on the test data from models averaging ensemble (three runs using all training data, 200 T1W image slices) (c)



Supplementary Figure S3: Examples of model failure in disease region segmentation. T1w image slices in oblique coronal plane (top) for three subjects with super-imposed models averaging ensemble rounded prediction (bottom). Subjects exhibit very abnormal bone, comprising either high fat content (left, middle) or sclerosis (right), leading to areas of 'missing' bone within the segmentations.



Supplementary Figure S4: Examples of discrepancies between readers for the cleaning step. The three discrepancies are denoted D1-D3 and shown on separate rows; for each, the STIR image (left column) and segmentations for the two readers (middle and right column) are shown. The green and red segmentations correspond to the higher and lower segmentation thresholds. In two cases (D1, D2), the disagreement was 'anatomical' and related to the presence of hyperintensity in the posterior ilium, which can be attributed to either inflammation or variations in normal bone composition. In one case (D3) the disagreement was 'artefactual' and related to the presence of faint, diffuse hyperintensity in the potentially-inflamed subchondral bone region, which was deemed entirely inflammatory by one reader and partly artefactual by the other.



8 References

1. Sieper J, Rudwaleit M, Baraliakos X, Brandt J, Braun J, Burgos-Vargas R, et al. The Assessment of SpondyloArthritis international Society (ASAS) handbook: A guide to assess spondyloarthritis. *Annals of the Rheumatic Diseases*. 2009;68(SUPPL. 2).
2. Bennett AN, Marzo-Ortega H, Kaur-Papadakis D, Rehman A. The use of magnetic resonance imaging in axial spondyloarthritis: Time to bridge the gap between radiologists and rheumatologists. *Journal of Rheumatology*. 2017;44(6):780–5.
3. Maksymowych WP, Pedersen SJ, Weber U, Weber U, Baraliakos X, MacHado PM, et al. Central reader evaluation of MRI scans of the sacroiliac joints from the ASAS classification cohort: Discrepancies with local readers and impact on the performance of the ASAS criteria. *Annals of the Rheumatic Diseases*. 2020 Jul 1;79(7):935–42.
4. Ez-Zaitouni Z, van Lunteren M, Bakker PAC, van den Berg R, Reijnierse M, Fagerli KM, et al. The influence of discrepant imaging judgements on the classification of axial spondyloarthritis is limited: A replication in the SpondyloArthritis Caught Early (SPACE) cohort. Vol. 77, *Annals of the Rheumatic Diseases*. BMJ Publishing Group; 2018.
5. van den Berg R, Lenczner G, Thévenin F, Claudepierre P, Feydy A, Reijnierse M, et al. Classification of axial SpA based on positive imaging (radiographs and/or MRI of the sacroiliac joints) by local rheumatologists or radiologists versus central trained readers in the DESIR cohort. *Annals of the Rheumatic Diseases*. 2015 Nov 1;74(11):2016–21.
6. Swami VG, Jaremko JL, Rumsey DG, Stimec J, Tse SML, Otopo TM, et al. Diagnostic accuracy of MRI-based sacroiliitis scoring systems: A systematic review. Vol. 212, *American Journal of Roentgenology*. American Roentgen Ray Society; 2019. p. 1112–25.
7. Hobby JL, Tr F, M Tom BD, Todd C, P Bearcroft PW, Dixon AK. Communication of doubt and certainty in radiological reports. Vol. 73, *The British Journal of Radiology*. 2000.

8. Sieper J, Rudwaleit M, Baraliakos X, Brandt J, Braun J, Burgos-Vargas R, et al. The Assessment of SpondyloArthritis international Society (ASAS) handbook: A guide to assess spondyloarthritis. *Annals of the Rheumatic Diseases*. 2009;68(Suppl. 2):ii1-44.
9. Lambert RGW, Bakker PAC, Van Der Heijde D, Weber U, Rudwaleit M, Hermann KGA, et al. Defining active sacroiliitis on MRI for classification of axial spondyloarthritis: Update by the ASAS MRI working group. *Annals of the Rheumatic Diseases*. 2016;75(11):1958–63.
10. Ronneberger O, Fischer P, Brox T. U-Net: Convolutional Networks for Biomedical Image Segmentation. 2015 May 18; Available from: <http://arxiv.org/abs/1505.04597>
11. Yushkevich PA, Piven J, Hazlett HC, Smith RG, Ho S, Gee JC, et al. User-guided 3D active contour segmentation of anatomical structures: Significantly improved efficiency and reliability. *Neuroimage*. 2006 Jul 1;31(3):1116–28.
12. Bishop CM. *Neural Networks for Pattern Recognition* CLARENDON PRESS • OXFORD 1995.
13. Kingma DP, Ba J. Adam: A Method for Stochastic Optimization. 2014 Dec 22; Available from: <http://arxiv.org/abs/1412.6980>
14. Ioffe S, Szegedy C. Batch Normalization: Accelerating Deep Network Training by Reducing Internal Covariate Shift. 2015 Feb 10; Available from: <http://arxiv.org/abs/1502.03167>
15. Billot B, Bocchetta M, Todd E, Dalca A v., Rohrer JD, Iglesias JE. Automated segmentation of the hypothalamus and associated subunits in brain MRI. *Neuroimage*. 2020 Dec 1;223.
16. Maksymowych WP, Inman RD, Salonen D, Dhillon SS, Williams M, Stone M, et al. Spondyloarthritis Research Consortium of Canada magnetic resonance imaging index for assessment of sacroiliac joint inflammation in ankylosing spondylitis. *Arthritis Care and Research*. 2005;53:703–9.
17. Isensee F, Jaeger PF, Kohl SAA, Petersen J, Maier-Hein KH. nnU-Net: a self-configuring method for deep learning-based biomedical image segmentation. *Nature Methods*. 2021 Feb 1;18(2):203–11.

18. Dumeer S, Einstein AJ. Coronary calcium scoring of CT attenuation correction scans: Automatic, manual, or visual? *Journal of Nuclear Cardiology*. 2018 Dec 15;25(6):2144–7.
19. Wolterink JM, Leiner T, de Vos BD, Coatrieux JL, Kelm BM, Kondo S, et al. An evaluation of automatic coronary artery calcium scoring methods with cardiac CT using the orCaScore framework. *Medical Physics*. 2016 May 1;43(5):2361–73.
20. Kucybała I, Tabor Z, Polak J, Urbanik A, Wojciechowski W. The semi-automated algorithm for the detection of bone marrow oedema lesions in patients with axial spondyloarthritis. *Rheumatology International*. 2020 Apr 1;40(4):625–33.
21. Chronaiou I, Thomsen RS, Huuse EM, Euceda LR, Pedersen SJ, Hoff M, et al. Quantifying bone marrow inflammatory edema in the spine and sacroiliac joints with thresholding. *BMC Musculoskeletal Disorders*. 2017 Nov 28;18(1).
22. Rzecki K, Kucybała I, Gut D, Jarosz A, Nabagło T, Tabor Z, et al. Fully automated algorithm for the detection of bone marrow oedema lesions in patients with axial spondyloarthritis – Feasibility study. *Biocybernetics and Biomedical Engineering*. 2021 Apr 1;41(2):833–53.